Electronic Supplementary Material (ESI) for Inorganic Chemistry Frontiers.
This journal is © the Partner Organisations 2022

Supporting Information

Chameleonic Metal-bound Isocyanides: π-Donating Cu^{I}-center Imparts a Nucleophilicity to the Isocyanide Carbon toward Halogen Bonding

Mikhail A. Kinzhalov, Daniil M. Ivanov, Anna A. Melekhova, Nadezhda A. Bokach, Rosa M. Gomila, Antonio Frontera, Vadim Yu. Kukushkin

Table of contents

S1. Materials and instrumentation

Reagents and materials used. Solvents, CuI, I_2, xylyl isocyanide, CHI_3 and $CHBr_3$ were obtained from commercial sources (Aldrich) and used as received, apart from CH_2Cl_2, which was purified by the conventional distillation over $CaCl_2$.

Instrumentation and methods. The high-resolution mass spectra were obtained on a Bruker micrOTOF spectrometer equipped with electrospray ionization (ESI) source and MeOH was used as the solvent. The instrument was operated at positive ion mode using *m/z* range of 50–3000. The most intensive peak in the isotopic pattern is reported. Infrared spectra (4000–400 cm^{-1}) were recorded on Shimadzu IRAffinity-1 FTIR spectrophotometer in KBr pellets. NMR spectra were recorded on Bruker AVANCE III 400 spectrometers in $CDCl_3$ at ambient temperature (at 400 and 100 MHz for ^1H and ^{13}C NMR, respectively). Chemical shifts are given in δ-values [ppm] referenced to the residual signals of undeuterated solvent ($CHCl_3$): δ 7.27 (^1H) and 77.0 (^{13}C).

X-ray Structure Determinations. Suitable single crystals were selected and mounted on a MiTeGen tip via crystallographic oil. Data were collected using Xcalibur, Eos diffractometer (monochromated Mo*Kα* radiation, λ = 0.71073 Å) at 100(2) K. In each case, the structure was solved with the ShelXT[1] structure solution program using Intrinsic Phasing and refined with the ShelXL[1] refinement package incorporated in the OLEX2 program package[2] using Least Squares minimization. Empirical absorption correction was applied in CrysAlisPro[3] program complex using spherical harmonics, implemented in SCALE3 ABSPACK scaling algorithm. The crystal data, data collection parameters, and structure refinement data are given in **Table S1**, a selected bond lengths and angles are given in **Table S2**. CCDC 1841440, 1841442, and 2092257 contain the supplementary crystallographic data for this paper. These data are provided free of charge by The Cambridge Crystallographic Data Centre.

Theoretical methods. The calculations of the monomers and dimers shown in **Figures 2**–**3** were performed at the DFT level theory using the PBE0[4]-D3[5] method, and the def2-TZVP basis set,[6] with the help of the Gaussian-16.[7] The topological analysis of the electron density distribution has been examined using the quantum theory of atoms in molecules (QTAIM) method developed by Bader[8] and the noncovalent interaction plot (NCIPlot)[9, 10] using the AIMAll program.[10] The estimation of the individual XB energies was done using the potential energy density (V_r) predictor as recently proposed in the literature ($E = 0.778V_r$)[11] for the PBE0 functional. The MEP surfaces were computed at the same level of theory by means of the Gaussian-16 program.[7] The PBE0 functional combined with D3 dispersion correction has been successfully used before to study halogen bonding interactions in a variety of solid-state systems and structures.[12-19] In some systems we have further validated the method by using the RI-MP2/def2-TZVPD level of theory[20] since it

has been demonstrated that it provides reliable energies, similar to gold standard CCSD(T) energies.[21] Latter calculations have been performed using the ORCA software.[22] The MP2 interaction energies were computed using the supramolecular approach, that is by subtracting the sum of the energies of the monomers to that of the dimer and using the X-ray coordinates.

The IRIplots[23] shown in the main text and the comparative NCI, IRI and IGM[24-27] plots shown below were computed using the MultiWFN program[28] and represented using the VMD program.[29] To do so, the wavefunction files obtained using the Turbomole 7.0 program[30] at the PBE0-D3/def2-TZVP level of theory were used as input files for their further analysis using the MultiWFN program.[28]

Single-point periodic DFT calculations using the mixed Gaussian/plane-wave[31] basis set and the PBE[32] -D3[5, 33] method for both studied crystals (1×1×1 cells) were performed in the CP2K-8.1 progam[34-40] and analyzed (QTAIM,[8] ELF[41, 42] and sign(λ_2)ρ[9, 10] projections) in MultiWFN program.[28] The short range variants of double-ζ polarization quality (for almost all atoms) or single-ζ (for C in aryl rings only to achieve 1.0×10^{-6} Hartree convergence for the self-consistent field cycle in the Γ-point approximation) Gaussian basis sets (DZVP-MOLOPT-SR-GTH[43] or SZV-MOLOPT-SR-GTH,[43] respectively) and a 350 Ry and a 50 Ry relative plane-wave cut-offs for the auxiliary grid, in conjunction with the Goedecker−Teter−Hutter[44-46] pseudopotentials were applied. Restrained electrostatic potential (RESP)[47, 48] atomic charges were calculated using REPEAT[47] method with constraints for all crystallographically dependent atoms of halomethanes and CuI_3 fragments to have the same RESP charges.

For periodic calculations in the CP2K program in the same schemes see refs.[49-57] For examples of single-point periodic calculations for σ-hole interactions see refs.[58-65]

S2. Synthetic work and characterization

Synthesis of [CuI(CNXyl)$_3$]. Xylyl isocyanide (134 mg, 1.02 mmol) was added to a suspension of CuI (65 mg, 0.34 mmol) in MeCN (20 mL), whereupon the reaction mixture was stirred for 40 min at RT until the complete homogenization. The resulting homogenous solution was evaporated under reduced pressure (20 mbar) at RT to dryness and the colorless residue that was formed was washed with Et_2O (two 2-mL portions) and then dried in air at RT. The yield of [CuI(CNXyl)$_3$] is 190 mg, 96%. Calcd (%) for $C_{27}H_{27}N_3CuI$: C 55.53, H 4.66, N 7.20; Found: C 55.76, H 4.63, N 7.22. HRESI$^+$ (MeOH, *m*/*z*): 325.0769 ([M–I–CNXyl]$^+$, calcd. 325.0761). FTIR, ν_{max} (KBr, cm^{-1}): 2137 s ν(C≡N). ^{1}H NMR ($CDCl_3$, δ): 2.49 (s, 6*H*, CH_3), 7.10 (d, $^3J_{H,H}$ = 7.5 Hz, 2*H*, *m*-H from xylyl), 7.21 (t, $^3J_{H,H}$ = 7.5 Hz, 1*H*, *p*-H from xylyl). ^{13}C NMR ($CDCl_3$, δ): 18.77 (CH_3), 126.06 (t, $^1J_{C,N}$ = 11.6 Hz, *ipso*-C from xylyl), 129.79 (*m*-C from xylyl), 129.20 (*o*-C from xylyl), 135.42 (*p*-C from xylyl), 151.98 ($C_{isocyanide}$).

Synthesis of [Cu(I)$_3$(CNXyl)$_3$]. Complex [CuI(CNXyl)$_3$] (190 mg, 0.33 mmol) and I_2 (83 mg, 0.33 mmol) were dissolved in CH_2Cl_2 at RT and left to stand for 30 min. Then the resulting homogenous brown solution was evaporated at RT at reduced pressure (20 mbar) until dryness with formation of brown residue. The yield of [Cu(I)$_3$(CNXyl)$_3$] is 256 mg, 94%. Calcd (%) for $C_{27}H_{27}N_3CuI_3$: C 38.71, H 3.25, N 5.02; Found: C 38.85, H 3.30, N 5.03. HRESI$^+$, *m*/*z*: 325.0758 ([M–I$_3$–CNXyl]$^+$, calcd. 325.0761), 456.1491 ([M–I$_3$]$^+$, calcd. 456.1601). FTIR, ν_{max} (KBr)/cm^{-1}: 2159 s ν(C≡N). ^{1}H NMR ($CDCl_3$, δ): 2.52 (s, 6*H*, CH_3), 7.15 (d, $^3J_{H,H}$ = 7.5 Hz, 2*H*, *m*-H from xylyl), 7.27 (t, $^3J_{H,H}$ = 7.5 Hz, 1*H*, *p*-H from xylyl). ^{13}C NMR ($CDCl_3$, δ): 19.00 (CH_3), 125.69 (t, $^1J_{C,N}$ = 13.1 Hz, *ipso*-C from xylyl), 128.08 (*m*-C from xylyl), 129.81 (*o*-C from xylyl), 135.58 (*p*-C from xylyl), 151.13 (t, $^1J_{C,N}$ = 14.6 Hz, $C_{isocyanide}$).

Crystal growth for the XRD study. Crystals of [CuI$_3$(CNXyl)$_3$]·CHX_3 (X = Br, I) were obtained by dissolution of a mixture of [CuI$_3$(CNXyl)$_3$] and CHX_3 (molar ratio 1:1) in CH_2Cl_2 at RT followed by slow evaporation of this solution at RT for 3 d.

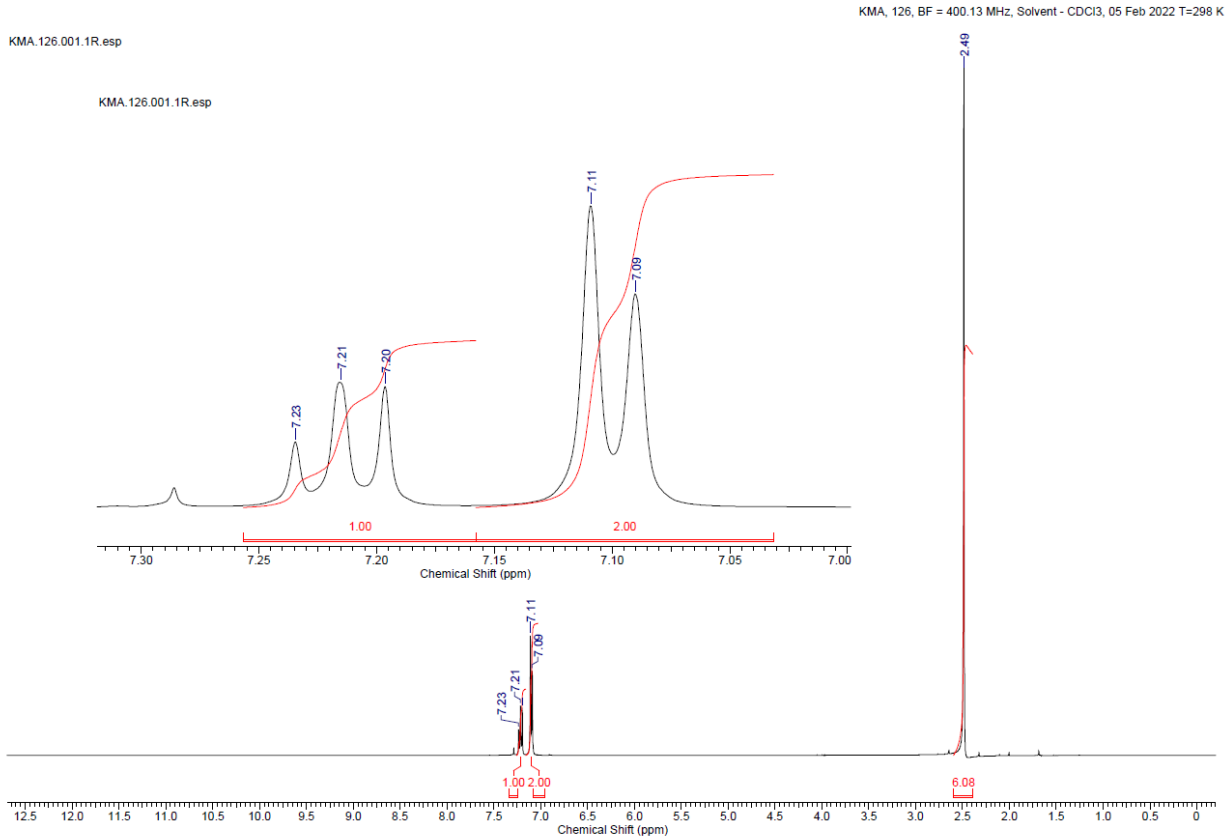

Figure S1. ^{1}H NMR spectrum of [CuI(CNXyl)$_3$] ($CDCl_3$, 400 MHz).

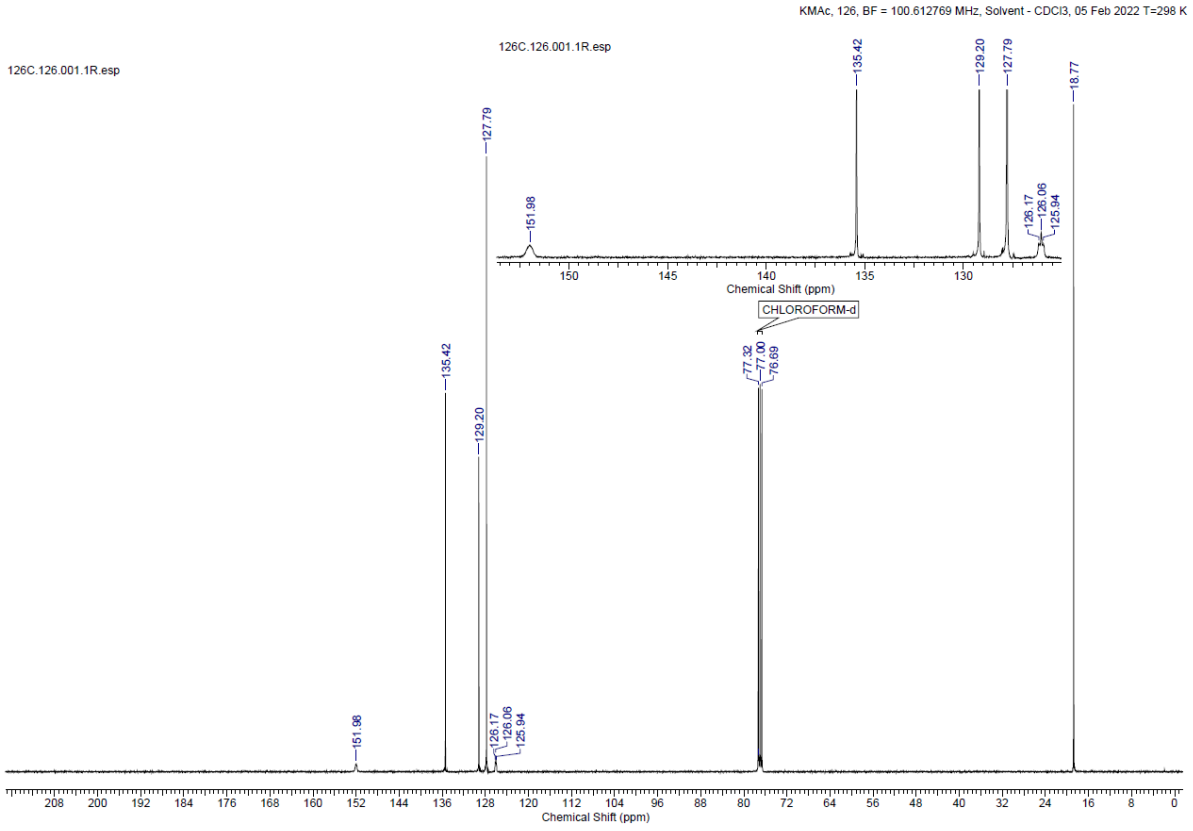

Figure S2. ^{13}C NMR spectrum of [CuI(CNXyl)$_3$] ($CDCl_3$, 100 MHz).

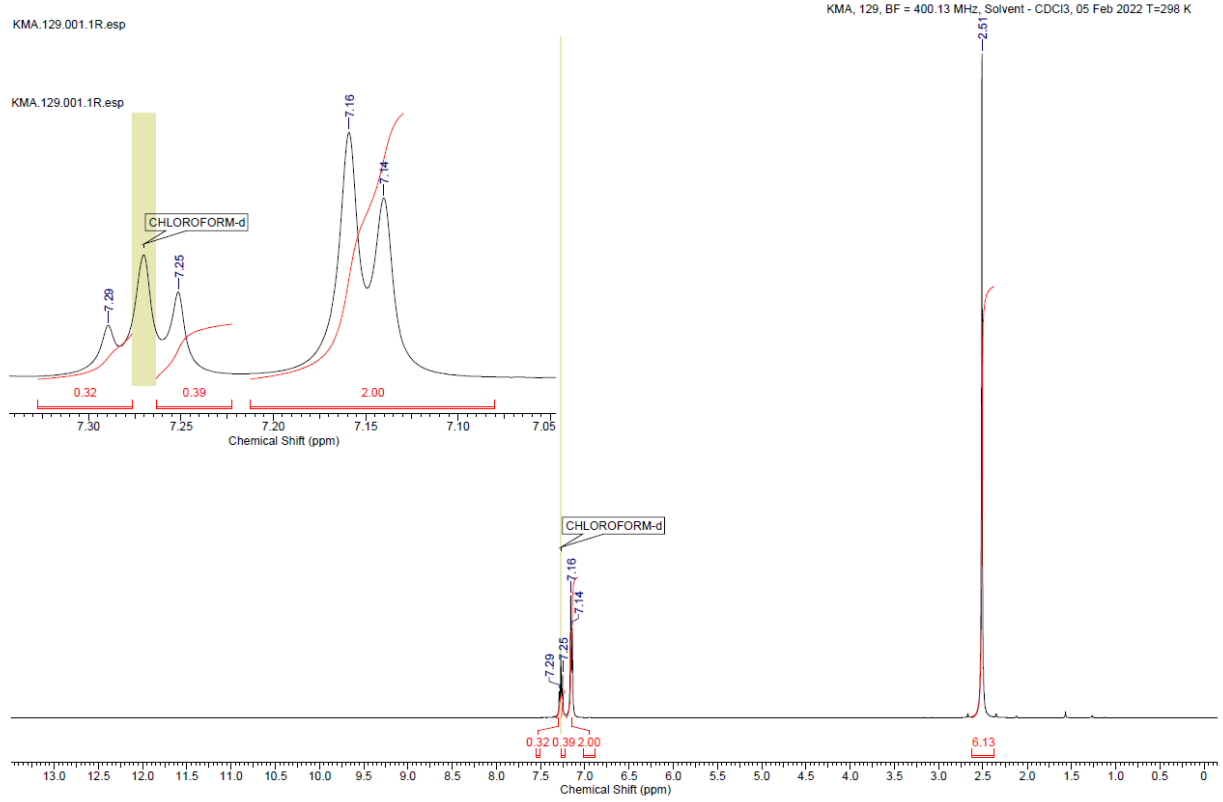

Figure S3. ^{1}H NMR spectrum of $[CuI_3(CNXyl)_3]$ ($CDCl_3$, 400 MHz).

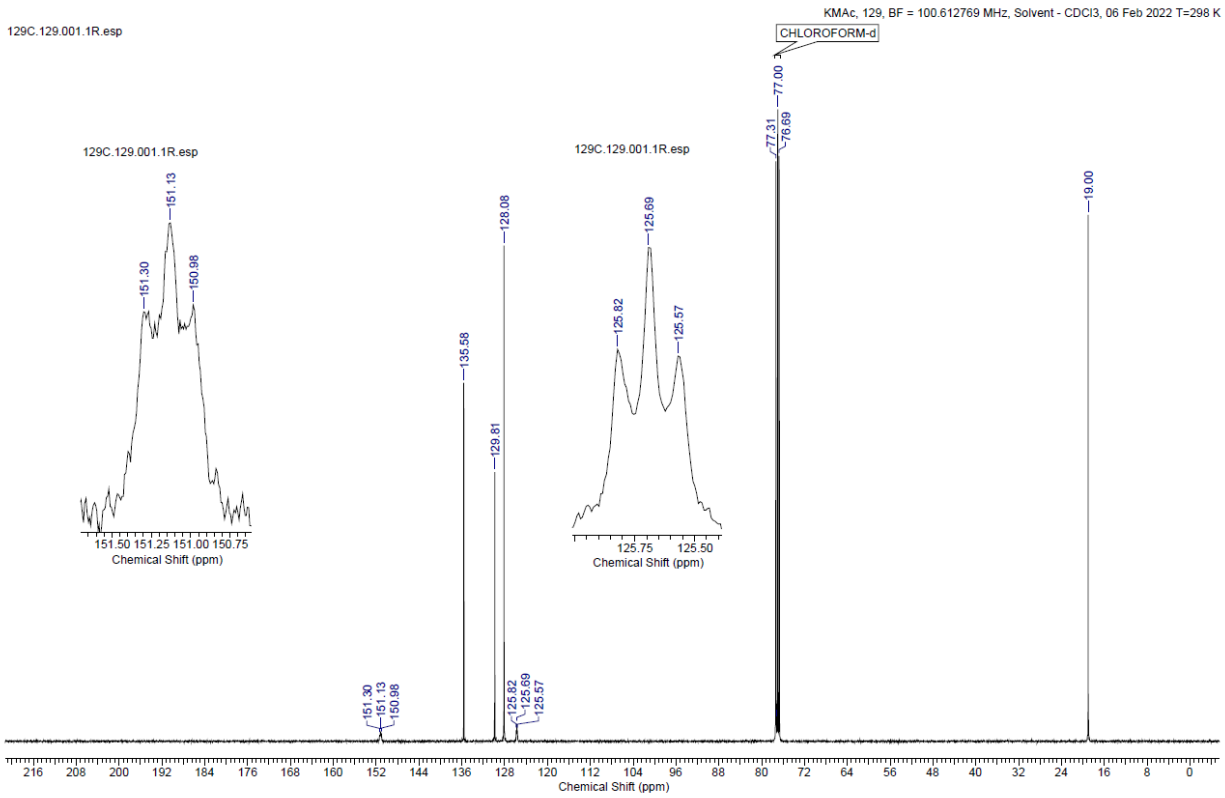

Figure S4. ^{13}C NMR spectrum of $[CuI_3(CNXyl)_3]$ ($CDCl_3$, 100 MHz).

S3. X-ray diffraction studies

Table S1. Crystal data and structure refinement for $[CuI_3(CNXyl)_3]$, $[CuI_3(CNXyl)_3]\cdot CHBr_3$, and $[CuI_3(CNXyl)_3]\cdot CHI_3$.

	$[CuI_3(CNXyl)_3]$	**$[CuI_3(CNXyl)_3]\cdot CHBr_3$**	**$[CuI_3(CNXyl)_3]\cdot CHI_3$**
CCDC	1841442	2092257	1841440
Empirical formula	$C_{27}H_{27}CuI_3N_3$	$C_{28}H_{28}Br_3CuI_3N_3$	$C_{28}H_{28}CuI_6N_3$
Formula weight	837.75	1090.50	1231.47
Temperature, K	100(1)	100(2)	100(1)
Crystal system	triclinic	monoclinic	monoclinic
Space group	$P\,\overline{1}$	$P2_1/c$	$P2_1/c$
a, Å	7.7060(3)	11.8924(3)	11.7870(3)
b, Å	9.4799(7)	17.3794(5)	17.6746(5)
c, Å	20.9583(14)	16.4283(4)	16.6827(4)
α, °	84.009(6)	90	90
β, °	88.633(4)	94.584(2)	93.467(3)
γ, °	80.703(5)	90	90
Volume, $Å^3$	1502.64(16)	3384.58(15)	3469.15(16)
Z	2	4	4
ρ_{calc}, g/cm^3	1.852	2.140	2.358
μ, mm^{-1}	3.827	6.945	5.991
F(000)	796.0	2040.0	2256.0
Crystal size, mm^3	0.13 × 0.12 × 0.10	0.37 × 0.28 × 0.23	0.18 × 0.12 × 0.12
Radiation	MoKα (λ = 0.71073)	Mo Kα (λ = 0.71073)	Mo Kα (λ = 0.71073)
2Θ range for data collection, °	5.564 to 54.998	4.986 to 54.994	5.218 to 52.996
Index ranges	–10 ≤ h ≤ 9, –11 ≤ k ≤ 12, –24 ≤ l ≤ 27	–14 ≤ h ≤ 14, –18 ≤ k ≤ 22, –20 ≤ l ≤ 21	–14 ≤ h ≤ 14, –20 ≤ k ≤ 22, –20 ≤ l ≤ 15
Reflections collected	13669	16381	16789
Independent reflections	6869 [R_{int} = 0.0285, R_{sigma} = 0.0422]	7390 [R_{int} = 0.0270, R_{sigma} = 0.0421]	7176 [R_{int} = 0.0231, R_{sigma} = 0.0292]
Data/restraints/-parameters	6869/0/313	7390/0/349	7176/0/349
Goodness-of-fit on F^2	1.095	1.108	1.056
Final *R* indexes [I≥2σ (I)]	R_1 = 0.0313, wR_2 = 0.0653	R_1 = 0.0332, wR_2 = 0.0681	R_1 = 0.0305, wR_2 = 0.0718
Final *R* indexes [all data]	R_1 = 0.0396, wR_2 = 0.0693	R_1 = 0.0478, wR_2 = 0.0734	R_1 = 0.0364, wR_2 = 0.0752
Largest diff. peak/hole, $e\cdot Å^{-3}$	1.26/–0.82	1.48/–0.72	3.22/–1.69

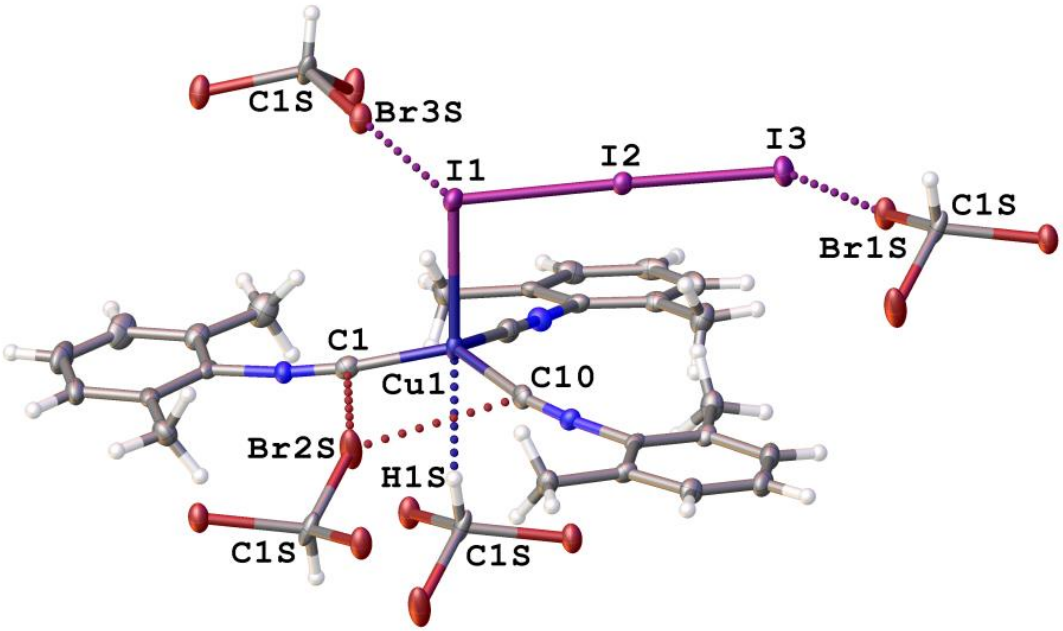

Figure S5. The structure of $[CuI_3(CNXyl)_3]\cdot CHBr_3$ with thermal ellipsoids at the 50% level.

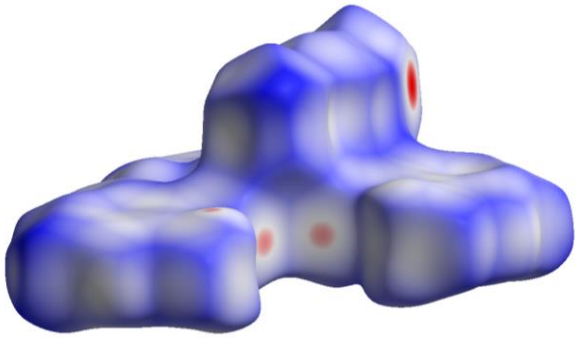

Figure S6. Hirshfeld surfaces for $[CuI_3(CNXyl)_3]$ in $[CuI_3(CNXyl)_3]\cdot CHI_3$

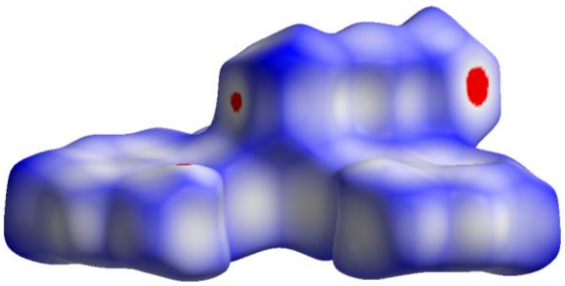

Figure S7. Hirshfeld surfaces for $[CuI_3(CNXyl)_3]$ in $[CuI_3(CNXyl)_3]\cdot CHBr_3$.

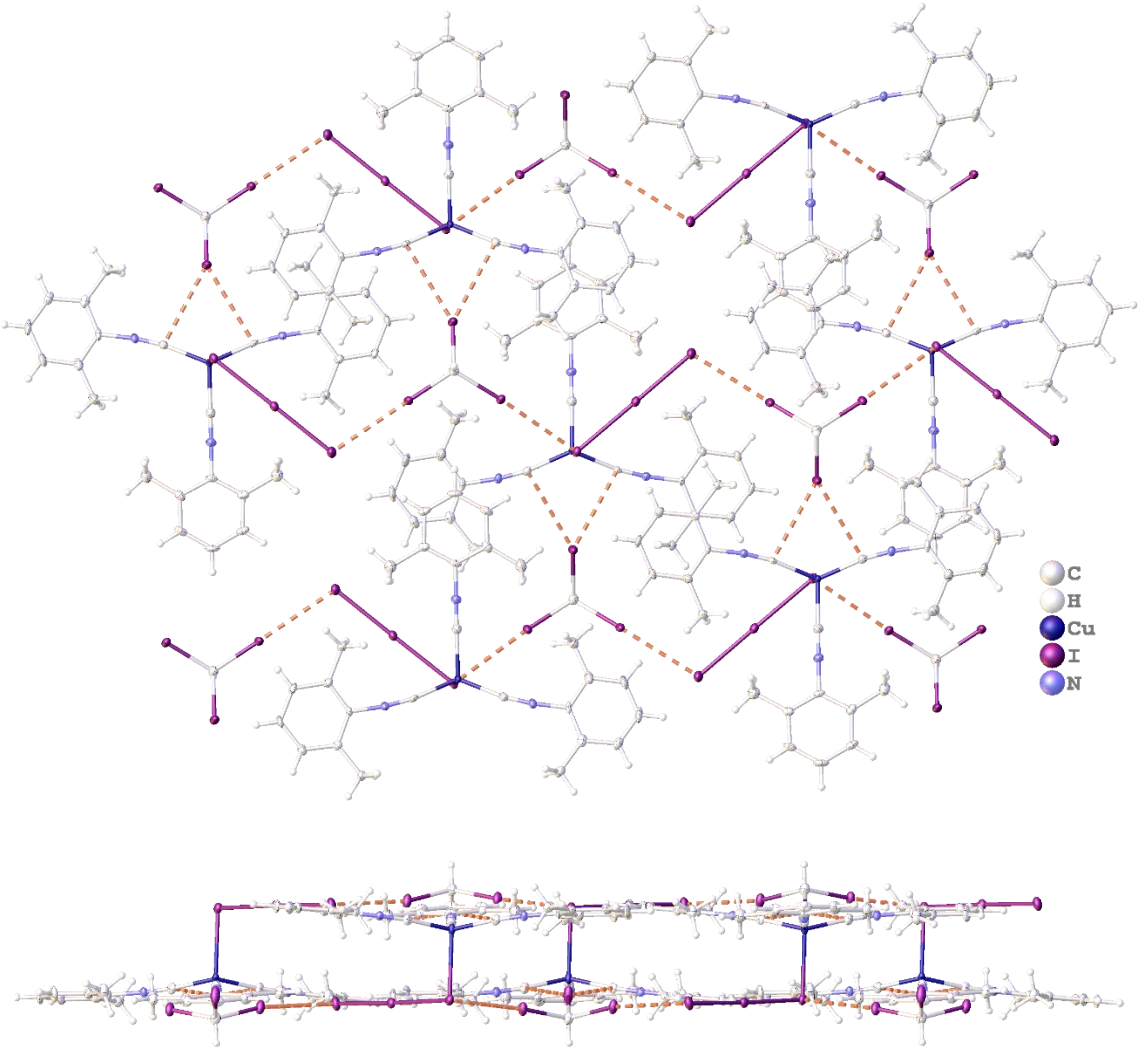

Figure S8. Crystal structure of $[CuI_3(CNXyl)_3]\cdot CHI_3$. CHI_3 molecule is bonded through one bifurcated halogen bond onto pairs of CN triple bonds and through two $I_{CHI_3}\cdots I_{I_3}$ halogen bonds with triiodide ligand interconnecting the molecules into 2D surface with each donor molecule binding to three acceptor molecules and vice versa. The crystal structure of $[CuI_3(CNXyl)_3]\cdot CHBr_3$ is similar.

Table S2. Selected bond lengths (Å) and angles (°) in $[CuI_3(CNXyl)_3]\cdot CHBr_3$ and $[CuI_3(CNXyl)_3]\cdot CHI_3$.

	$[CuI_3(CNXyl)_3]\cdot CHBr_3$	$[CuI_3(CNXyl)_3]\cdot CHI_3$
Bond lengths, Å		
Cu1–I1	2.7545(6)	2.7800(6)
Cu1–C1	1.935(5)	1.933(5)
Cu1–C10	1.945(5)	1.944(5)
Cu1–C19	1.968(5)	1.953(5)
N1–C1	1.152(6)	1.163(6)
N2–C10	1.147(6)	1.162(6)
N3–C19	1.144(6)	1.160(6)
I1–I2	2.9993(4)	3.0011(4)
I2–I3	2.7545(6)	2.8582(4)
Angle, °		
Cu1–C1–N1	170.8(4)	170.4(4)
Cu1–C10–N2	170.1(4)	170.3(4)
Cu1–C19–N3	178.4(5)	179.6(5)
C1–Cu1–C10	127.2(2)	129.0(2)
C10–Cu1–C19	110.04(19)	109.9(2)
C1–Cu1–C19	111.5(2)	111.1(2)
C1–N1–C2	171.7(5)	172.6(5)
C10–N2–C11	173.2(5)	173.6(5)
C19–N3–C20	178.2(5)	178.5(5)
Cu1–I1–I2	92.497(15)	92.188(15)
I1–I2–I3	178.632(14)	178.398(14)

Table S3. Geometric parameters of HaBs and H···Cu H-bonding in the crystal structures of in $[CuI_3(CNXyl)_3]\cdot CHBr_3$ and $[CuI_3(CNXyl)_3]\cdot CHI_3$.

Structure	Contact	d(X···Y), Å	R_{Bondi}[a]	$R_{Alv.}$[b]	∠ (C−X···Y), °
$HX_2C(\mu_2\text{-}X)\cdots(\underline{C}-Cu-\underline{C})$ BHaBs					
$[CuI_3(CNXyl)_3]\cdot CHBr_3$	C1S–Br2S···C1	3.582(5)	1.01	0.99	142.6(2)
$[CuI_3(CNXyl)_3]\cdot CHI_3$	C1S–I2S···C1	3.546(5)	0.96	0.93	145.35(15)
$[CuI_3(CNXyl)_3]\cdot CHBr_3$	C1S–Br2S···C10	3.585(5)	1.01	0.99	141.4(2)
$[CuI_3(CNXyl)_3]\cdot CHI_3$	C1S–I2S···C10	3.559(5)	0.96	0.93	144.23(16)
$HX_2C-X\cdots(\underline{I}-I-I-Cu)$					
$[CuI_3(CNXyl)_3]\cdot CHBr_3$	C1S–Br1S···I3	3.5893(6)	0.94	0.92	175.2(2)
$[CuI_3(CNXyl)_3]\cdot CHI_3$	C1S–I1S···I3	3.5867(5)	0.90	0.88	170.12(13)
$HX_2C-X\cdots(I-I-\underline{I}-Cu)$					
$[CuI_3(CNXyl)_3]\cdot CHBr_3$	C1S–Br3S···I1	3.6315(6)	0.95	0.93	176.0(1)
$[CuI_3(CNXyl)_3]\cdot CHI_3$	C1S–I3S···I1	3.5901(5)	0.90	0.88	174.75(14)
$X_3C-H\cdots Cu$					
$[CuI_3(CNXyl)_3]\cdot CHBr_3$	C1S–H1S···Cu1	2.5917	0.99	0.72	171
$[CuI_3(CNXyl)_3]\cdot CHI_3$	C1S–H1S···Cu1	2.57	0.98	0.72	176

[a] R_{Bondi} is a ratio between the interatomic distance and sum of Bondi vdW radii.[66]

[b] $R_{Alv.}$ is a ratio between the interatomic distance and sum of Alvarez vdW radii.[67]

The $HX_2C-X\cdots(\underline{I}-I-I-Cu)$ and $HX_2C-X\cdots(I-I-\underline{I}-Cu)$ halogen bonding. In the structures of $[CuI_3(CNXyl)_3]\cdot CHX_3$, the $HX_2C-X\cdots I_3Cu$ short contacts between an X atom from CHX_3 and I atom from triiodide ligand comprises ca. 90% of $\sum_{vdW}$; the corresponding angle around the X center of CHX_3 is close to 180° ($\Theta_{C-I\cdots I}$ = 170.12(13)–174.75(14)°; **Table S1**). These data along with the data on a surface maximum $V_S(\mathbf{r})_{max}$ (18–26 kcal mol^{-1}) located on the σ-hole of the X atoms in CHX_3 indicate that this short contact is due to HaB, according to the IUPAC criteria for Type II halogen-halogen interactions[68] and the X atom from CHX_3 acts as σ-hole donor which interacts with an electron belt of triiodide ligand. The second X atom of CHX_3 exhibits the HaB with an I of the triiodide from another complex and one CHX_3 behaves as a bridge linking two neighboring complexes. Correspondingly, in this structure, CHX_3 act as bifunctional HaB/HaB donors and the triiodide functions as a bifunctional linear HaB/HaB acceptor, whose interplay gives zig-zag 1D chains held by HaB.

The $X_3C-H\cdots Cu$ hydrogen bonding. The position of the hydrogen atom of CHX_3 indicates the presence of H···Cu interaction. The H···Cu distances are 2.59 Å and 2.57 Å for $[CuI_3(CNXyl)_3]\cdot CHBr_3$ and $[CuI_3(CNXyl)_3]\cdot CHI_3$ respectively that is less than the sum of the vdw radii (ca. 98–99% of $\sum_{vdW}$). The C–H···Cu angle is close to linear (171.0–176.0°; **Table S3**).

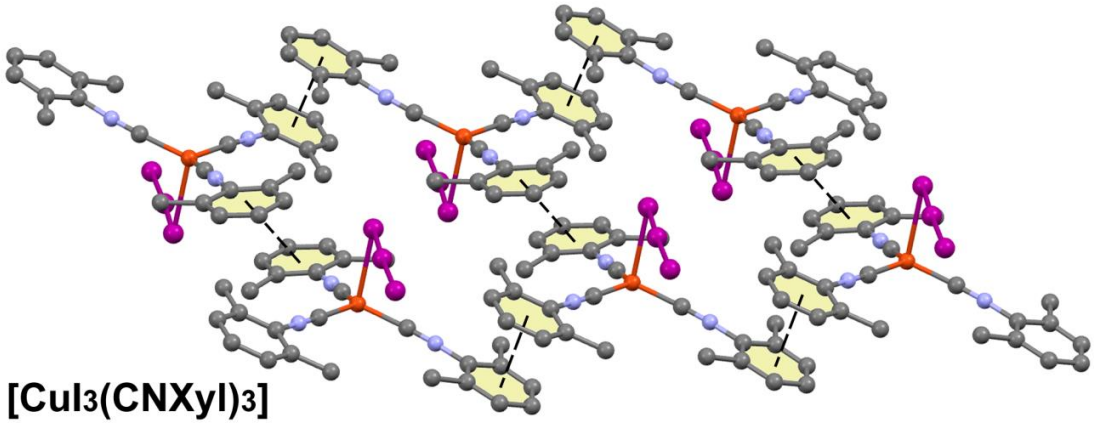

Figure S9. Partial view of the X-ray structure of $[CuI_3(CNXyl)_3]$ with indication of the dominant π···π stacking interactions.

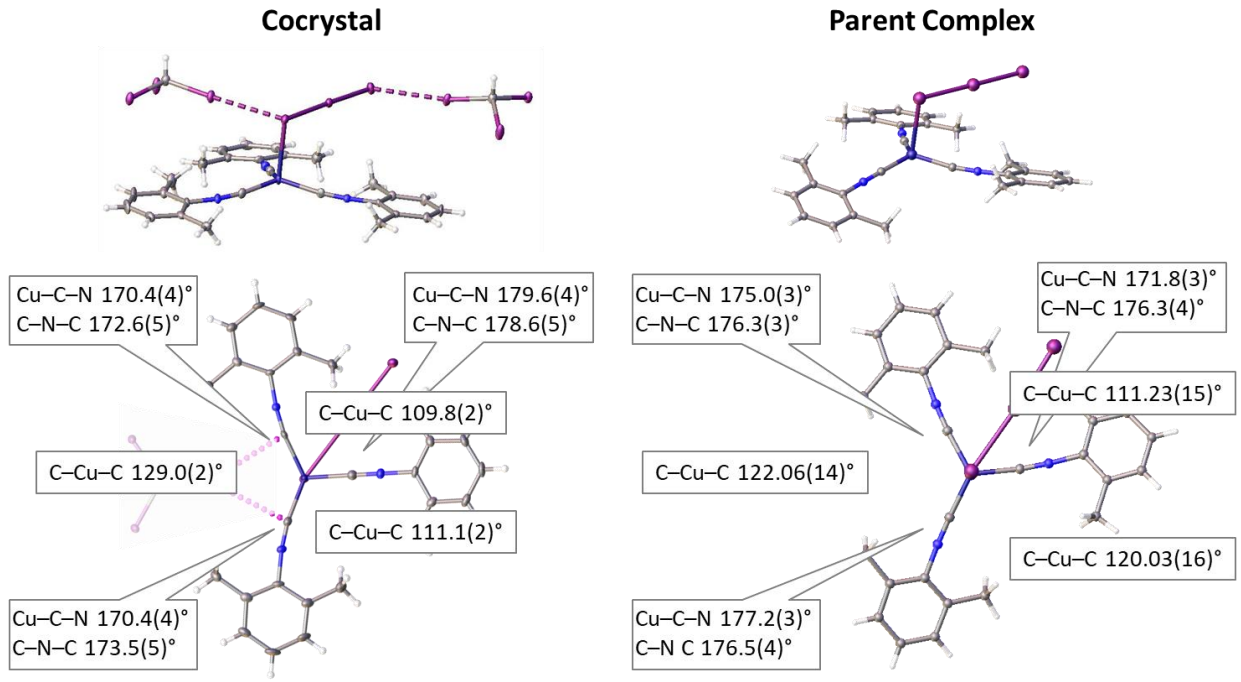

Figure S10. The comparison of the crystal structures of $[CuI_3(CNXyl)_3]\cdot CHI_3$ with those of the unassociated $[CuI_3(CNXyl)_3]$.

S4. Bromoform and iodoform as HaB donors

CHX_3 have been conventionally studied as HaB donors to give a number of reports focused on CHX_3-involving HaBs with halide anions,[69-73] halide[74-77] and pseudohalide [78-80] ligands, with other *N*- [81-85] and *S*-nucleophiles (for CHI_3 refs.[86-89] and for $CHBr_3$ ref.[90]), $CHBr_3$ [75, 91, 92] and CHI_3 [69, 75, 76, 85, 93] HaB self-association, and even with Pd^{II} [75] and Pt^{II} [75, 76] metal centers. Bromoform was also employed as HaB donor toward O-nucleophiles,[73, 92, 94-97] whereas iodoform was found to be I-electrophile toward Se-nucleophilic center.[98]

S5. Theoretical calculations

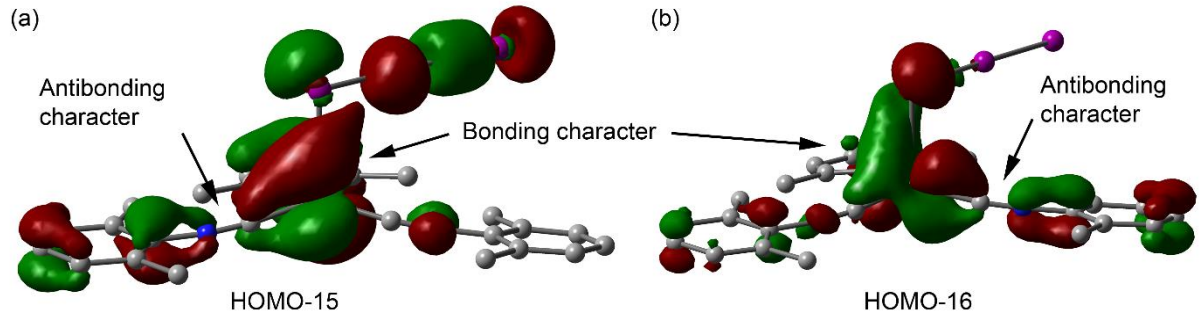

Figure S11. Surface plots of the HOMO-15 and LUMO-16 for [$CuI_3(CNXyl)_3$].

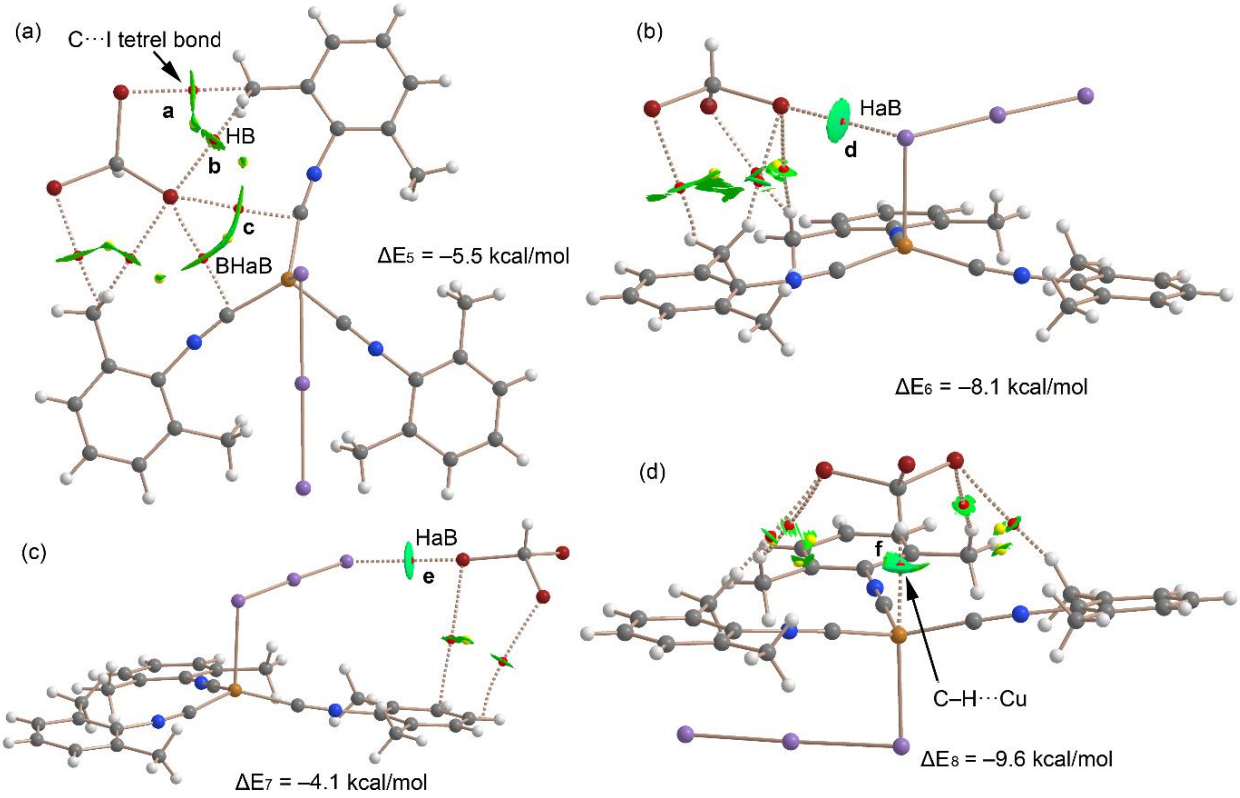

Figure S12. QTAIM distribution of bond and ring CP (red and yellow spheres, respectively) and bond paths for the BHaB dimer (*a*), HaB dimers (*b*,*c*), and H-bond dimer (*d*) of [$CuI_3(CNXyl)_3$]·$CHBr_3$. The NCIplot isosurfaces are also represented using 0.4 au isosurface and a gradient cut-off of 0.04 au. The color range is -0.04 au $\leq \text{sign}(\lambda_2)\rho \leq 0.04$. Only CPs and NCIplot surfaces characterizing intermolecular interactions are represented for clarity.

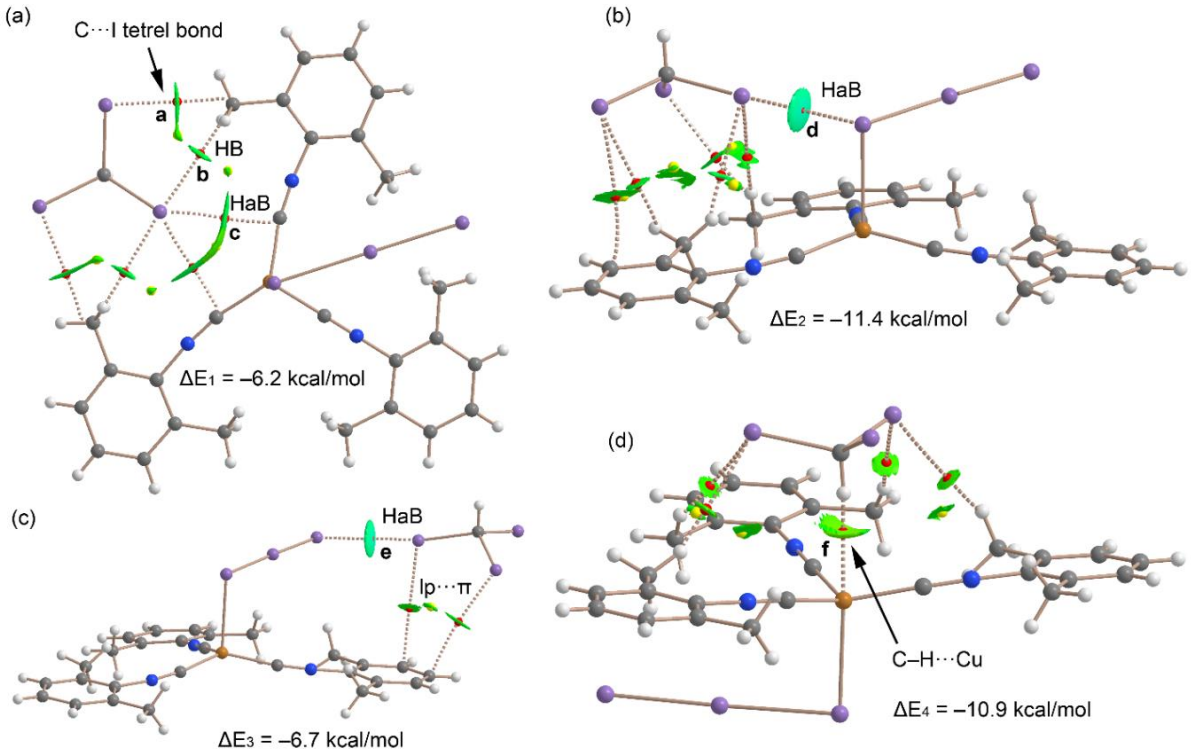

Figure S13. QTAIM distribution of bond and ring CP (red and yellow spheres, respectively) and bond paths for the BHaB dimer (*a*), HaB dimers (*b*,*c*), and H-bond dimer (*d*) of compound $[CuI_3(CNXyl)_3]\cdot CHI_3$. The NCIplot isosurfaces are also represented using 0.4 au isosurface and a gradient cut-off of 0.04 au. The color range is –0.04 au ≤ sign(λ_2)ρ ≤ 0.04. Only CPs and NCIplot surfaces characterizing intermolecular interactions are represented for clarity.

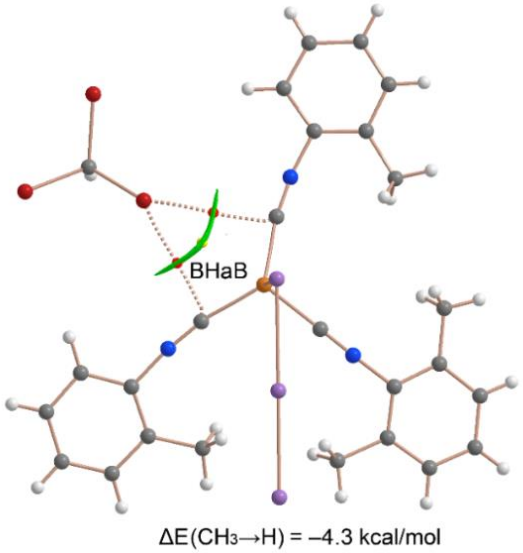

Figure S14. QTAIM distribution of bond and ring CP (red and yellow spheres, respectively) and bond paths for the mutated model of the $[CuI_3(CNXyl)_3]\cdot CHBr_3$ adduct formed by BHaB. The NCIplot isosurfaces are also represented using 0.4 au isosurface and a gradient cut-off of 0.04 au. The color range is –0.04 au ≤ sign(λ_2)ρ ≤ 0.04 au. Only CPs and NCIplot surfaces characterizing intermolecular interactions are represented for clarity.

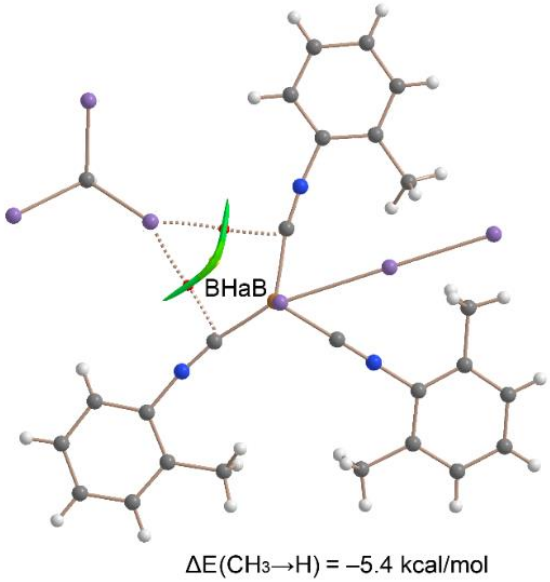

Figure S15. QTAIM distribution of bond and ring CP (red and yellow spheres, respectively) and bond paths for the mutated model of the $[CuI_3(CNXyl)_3]\cdot CHI_3$ adduct formed by BHaB. The NCIplot isosurfaces are also represented using 0.4 au isosurface and a gradient cut-off of 0.04 au. The color range is –0.04 au ≤ sign(λ_2)ρ ≤ 0.04 au. Only CPs and NCIplot surfaces characterizing intermolecular interactions are represented for clarity.

In **Table S4**, we summarized the QTAIM values at the bond CPs labelled as "**a**–**f**" in **Figures S12**–**S13** and the associated interaction energies based on the potential energy density (V_r) predictor,[99] apart from the tetrel bond where the V_r predictor value is not available.

For the halogen-bonded dimer involving I1 (**Figures 3** and **S5** for atom labelling), the HaB (–2.29 and –3.22 kcal/mol, in $[CuI_3(CNXyl)_3]\cdot CHBr_3$ and $[CuI_3(CNXyl)_3]\cdot CHI_3$, respectively, CPs labelled as **d**) is stronger than the BHaB, in agreement with the NCIplot surface analysis. Moreover, the difference between these energies and the respective dimerization energies (ΔE_6 = –8.1 kcal/mol and ΔE_2 = –11.4 kcal/mol) can be attributed to the rest of the H···X contacts (**Figures S12b** and **S13b**). For the halogen-bonded dimer involving I3, the HaB (–2.50 and –3.22 kcal/mol, in $[CuI_3(CNXyl)_3]\cdot CHBr_3$ and $[CuI_3(CNXyl)_3]\cdot CHI_3$, respectively, CPs labelled as **e**) is very similar to the I3S···I1 dimer. Moreover, the difference between these energies and the respective dimerization energies (ΔE_7 = –4.1 kcal/mol and ΔE_3 = –6.4 kcal/mol) can be attributed to the lp···π interactions (**Figures S12c** and **S13c**). Finally, the energies of the C–H···Cu contacts are small –1.81 ($[CuI_3(CNXyl)_3]\cdot CHBr_3$) and –1.91 kcal/mol ($[CuI_3(CNXyl)_3]\cdot CHI_3$; CPs labelled as **f**) in line with the small MEP value observed at the Cu atom (–2.5 kcal/mol). Therefore, this dimer is likely dominated by the formation of the four C–H···I HBs.

Table S4. QTAIM parameters (ρ, $\nabla^2\rho$, V_r, G_r and H_r in au) at the bond CPs of X···C,I HaBs, H···Cu and H···X HBs for the dimers of $[CuI_3(CNXyl)_3]\cdot CHBr_3$ and $[CuI_3(CNXyl)_3]\cdot CHI_3$ (see **Figures 3** and **S5** for labelling).

CP	ρ	$\nabla^2\rho$	V_r	G_r	H_r	E_{int}
$[CuI_3(CNXyl)_3]\cdot CHBr_3$						
a	0.0053	0.0196	–0.0028	0.0039	0.0010	n.a.
b	0.0048	0.0170	–0.0023	0.0033	0.0010	–0.72
c	0.0050	0.0158	–0.0021	0.0030	0.0009	–1.02
d	0.0105	0.0253	–0.0047	0.0055	0.0008	–2.29
e	0.0110	0.0274	–0.0052	0.0060	0.0008	–2.50
f	0.0105	0.0240	–0.0058	0.0059	0.0001	–1.81
$[CuI_3(CNXyl)_3]\cdot CHI_3$						
a	0.0052	0.0171	–0.0026	0.0034	0.0008	n.a.
b	0.0067	0.0181	–0.0028	0.0037	0.0009	–0.88
c	0.0070	0.0191	–0.0030	0.0039	0.0009	–1.46
d	0.0145	0.0294	–0.0066	0.0070	0.0004	–3.22
e	0.0143	0.0301	–0.0066	0.0071	0.0005	–3.22
f	0.0108	0.0255	–0.0061	0.0062	0.0001	–1.91

NCIPlot, IRIPlot and IGMplot of (μ2-X)···(NC−Cu−CN) heterodimers

Figures S16–S17 show the results from the three analyses focused on the (μ2-X)···(C−Cu−C) dimers. All three methods provide similar information regarding the interactions, showing blue isosurfaces between the halogen atom and the C-atom of the isocyano group, coincident to the location of the bond CPs (red spheres) interconnecting the I,Br and C-atoms. Interestingly, these three analyses also reveal that the interaction between the Cu-atom and the halogen atom is repulsive since yellow/red isosurfaces also located between the Br,I-atoms and the Cu atom coincident to the ring CPs (yellow spheres).

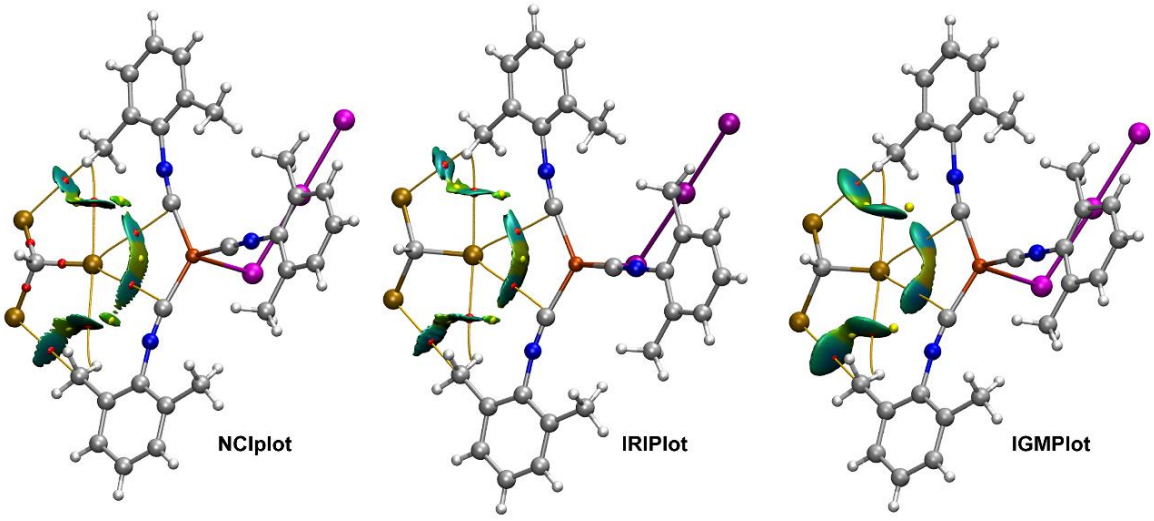

Figure S16. NCI (left), IRI (middle) and IGM (right) plots of the $[CuI_3(CNXyl)_3]\cdot CHBr_3$ dimer at the PBE0-D3/def2-TZVP level of theory. Color scale used for the three plots -0.01 a.u. $\leq (\text{sign}\lambda_2)\rho \leq 0.01$ a.u.

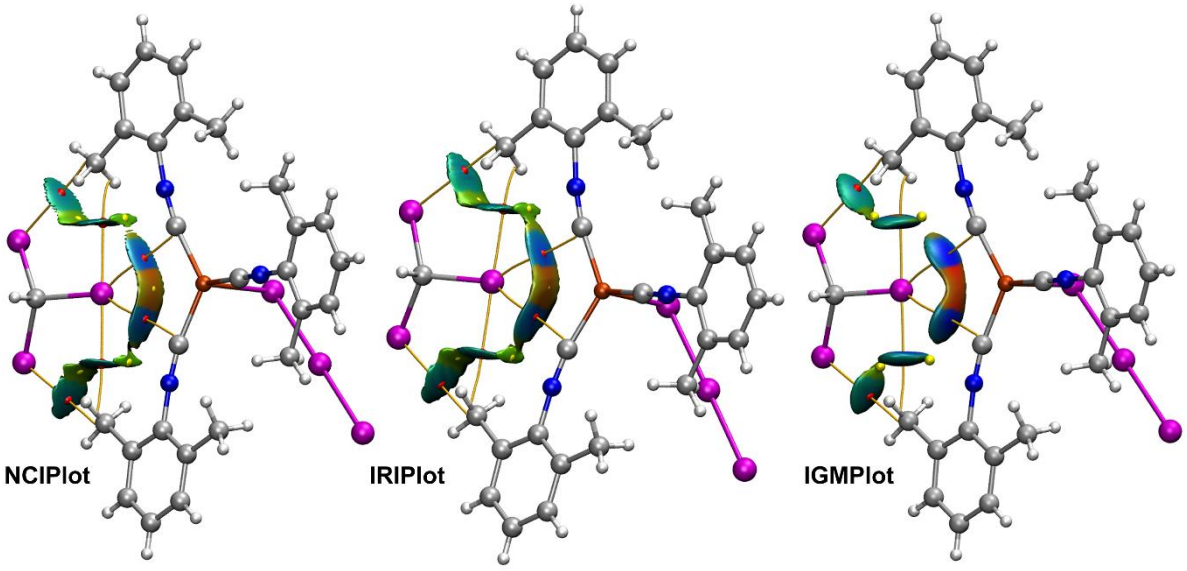

Figure S17. NCI (left), IRI (middle) and IGM (right) plots of the $[CuI_3(CNXyl)_3]\cdot CHI_3$ dimer at the PBE0-D3/def2-TZVP level of theory. Color scale used for the two plots -0.01 a.u. $\leq (sign\lambda_2)\rho \leq 0.01$ a.u.

We used the intrinsic bond strength index (IBSI) to measure relative strength of the bifurcated HaBs. The intrinsic bond strength index (IBSI) proposed in ref. [27] has certain ability in characterizing strength of covalent bonds, however their ability to characterize noncovalent interaction is not proven yet. These calculations were carried out at the PBE0-D3/def2-TZVP level of theory and using the high-quality integration grid to increase the numerical accuracy. The δg values used in the equation to calculate the IBSI index were also calculated since it has been demonstrated that they correlate with bonding dissociation energies in covalent bonds. However, it is not clear if this correlation can be transferred to weak interactions. The IBSI and δg values for the Br,I···C and Br,I···Cu pairs are summarized in **Table S5**. In line with the energetic results, both the IBSI and atomic pair δg index values are larger for the I···C contacts, which are stronger energetically. Both parameters are smaller for the Br,I···Cu pairs, thus confirming that the interaction is basically with the C-atoms of the isocyano groups.

Table S5. δg, IBSI and IBSIW values for the Br···[C–Cu–C] and I···[C–Cu–C] contacts using the PBE0-D3/def2-TZVP wavefunction

Atom1	**Atom2**	**Dist (Å)**	**δg**	**IBSI**	**IBSIW**
$[CuI_3(CNXyl)_3]\cdot CHBr_3$					
Br	Cu	3.9391	0.08127	0.01277	0.511671
Br	C(CN)	3.5854	0.09666	0.01833	0.750364
Br	C(CN)	3.5822	0.08835	0.01678	0.684239
$[CuI_3(CNXyl)_3]\cdot CHI_3$					
I	Cu	3.8766	0.12047	0.01954	0.782569
I	C	3.5455	0.12615	0.02446	0.996742
I	C	3.5593	0.13557	0.02608	1.067231

Table S5 also reports the IBSIW (intrinsic bond strength index for weak interactions) This index may have stronger relation with noncovalent interaction strength than atom pair δg index. The IBSIW values of **Table S5** are in line with the IBSI ones and corroborate that the I···C contacts are the stronger than the Br···C ones. Moreover, the I···C and Br···C are the atomic pairs (apart from covalent bond) with higher δg, IBSI, and IBSIW values of all possible atoms pair combinations, thus confirming their crucial role in the stabilization of the supramolecular dimers.

Periodic calculations: comparison with cluster calculations

Since calculations with periodic boundary conditions (CP2K-8.1, PBE-D3/(DZVP/SZV)-SR-MOLOPT-GTH and for the isolated clusters (Gaussian-16, PBE0-D3/def2-TZVP) were performed in the different schemes and programs, the comparison is highly required. The QTAIM analysis was made for both *crystal* and *cluster* models, and parameters of electron density in (3, –1) BCPs of the most important noncovalent interactions were calculated (**Table S6**). Note that the models from both methodologies not only showed all required BCPs confirming the corresponding interactions, but also demonstrated almost the same ρ, $\nabla^2\rho$, V_r, and G_r values with the largest difference in $\nabla^2\rho$.

Table S6. QTAIM parameters (ρ, $\nabla^2\rho$, V_r, G_r in au) at the bond CPs of X···C,I HaBs and H···Cu HBs for *crystal* or *cluster* models of $[CuI_3(CNXyl)_3]\cdot CHBr_3$ and $[CuI_3(CNXyl)_3]\cdot CHI_3$ (see **Figures 1** and **S5** for labelling).

Interaction	object	ρ	$\nabla^2\rho$	V_r	G_r
$[CuI_3(CNXyl)_3]\cdot CHBr_3$					
Br2S···C1	*cluster*	0.0050	0.0158	–0.0021	0.0030
	crystal	0.0049	0.0153	–0.0018	0.0028
Br2S···C10	*cluster*	0.0050	0.0157	–0.0021	0.0030
	crystal	0.0049	0.0153	–0.0018	0.0028
Br3S···I1	*cluster*	0.0105	0.0253	–0.0047	0.0055
	crystal	0.0099	0.0272	–0.0045	0.0057
Br1S···I3	*cluster*	0.0110	0.0274	–0.0052	0.0060
	crystal	0.0105	0.0289	–0.0050	0.0061
H1S···Cu1	*cluster*	0.0105	0.0240	–0.0058	0.0059
	crystal	0.0105	0.0281	–0.0055	0.0062
$[CuI_3(CNXyl)_3]\cdot CHI_3$					
I2S···C1	*cluster*	0.0071	0.0195	–0.0031	0.0040
	crystal	0.0071	0.0195	–0.0028	0.0038
I2S···C10	*cluster*	0.0070	0.0191	–0.0030	0.0039
	crystal	0.0069	0.0191	–0.0027	0.0037
I3S···I1	*cluster*	0.0145	0.0294	–0.0066	0.0070
	crystal	0.0138	0.0301	–0.0062	0.0068
I1S···I3	*cluster*	0.0143	0.0301	–0.0066	0.0071
	crystal	0.0139	0.0302	–0.0062	0.0068
H1S···Cu1	*cluster*	0.0108	0.0255	–0.0061	0.0062
	crystal	0.0108	0.0294	–0.0059	0.0066

Although QTAIM can detect almost all noncovalent interactions, in some cases the following NCI analysis is required. Since the 3D visualization of NCI in *crystal* model is not as clear and convincing as for isolated clusters, the sign(λ_2)ρ projections together with topological analysis of electron density were drawn for the most important C−X···(C,C) interactions in both *crystal* and *cluster* models (**Figure S18**).

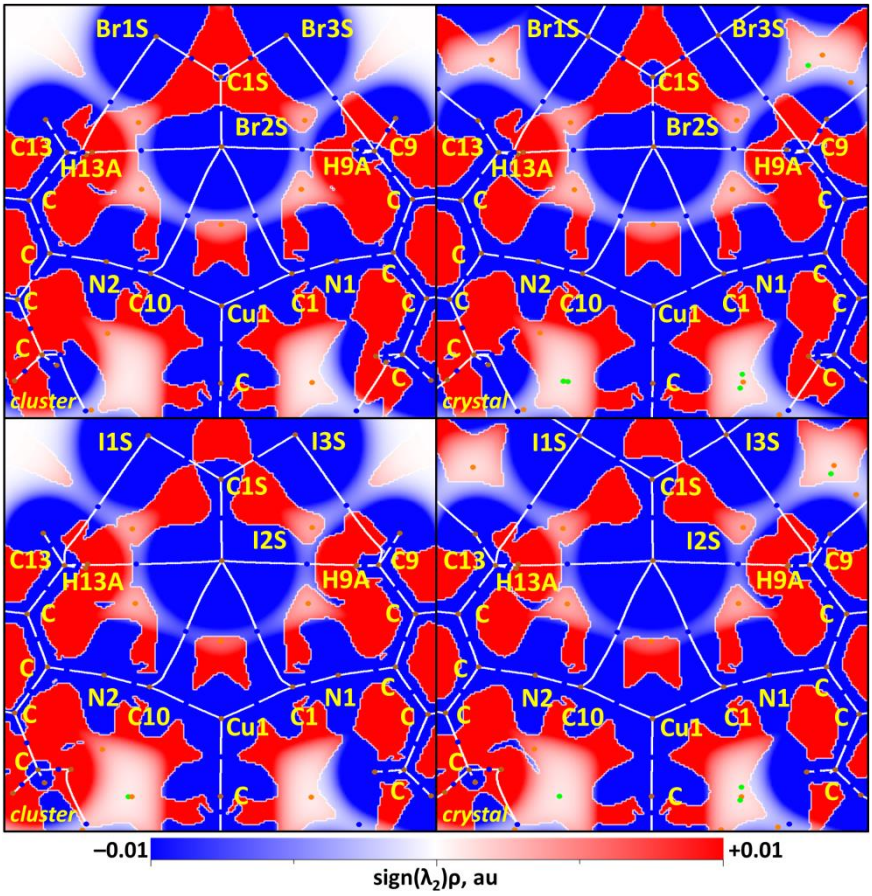

Figure S18. Sign(λ_2)ρ projections and bond paths (white lines), bond CPs (blue dots), nuclear CPs (brown dots), ring CPs (orange dots), and cell CPs (green dots), for the C1S−X2S···(C1,C10) HaBs in the cluster (left) and crystal (right) models of $[CuI_3(CNXyl)_3]\cdot CHBr_3$ (upper) and $[CuI_3(CNXyl)_3]\cdot CHI_3$ (lower).

The sign(λ_2)ρ areas are blue (denoting attractive interaction) between the X-atom and the C-atoms of the [C−Cu−C] core in all cases, coincident to the location of the BCPs. In contrast, a red colored areas are observed between the Cu center and the interacting X-atom or between X and N isocyanide atoms, denoting a repulsive interaction. Thus both *crystal* and *cluster* models confirmed the halogen-carbon-centered attractive interactions between haloform and isocyanide moieties.

The philicities of noncovalently interacting partners can be determined by electron localization function projections with critical points and bond paths from QTAIM electron density topology, which were drawn for both *crystal* and *cluster* models. In all cases, the X···C bond paths lie down between two LPs areas of X atoms and passes through the C LP areas; the Cu−C coordination bond paths lie in the same areas. Note that the differences between ELF areas around X atoms in *cluster* and *crystal* models can be explained by exploring the large Goedecker−Teter−Hutter pseudopotentials in the latter cases, and only valent shells around X atoms were calculated. Nevertheless, the inspection of the ELF data proves the BHaB nature of

the $HX_2C(\mu_2\text{-}X)\cdots(C{-}Cu{-}C)$ interactions, where the C-atoms of the coordinated isocyanides in $[CuI_3(CNXyl)_3]$ function as nucleophilic partners of the BHaB, while the X centers of CHX_3 serve as electrophiles.

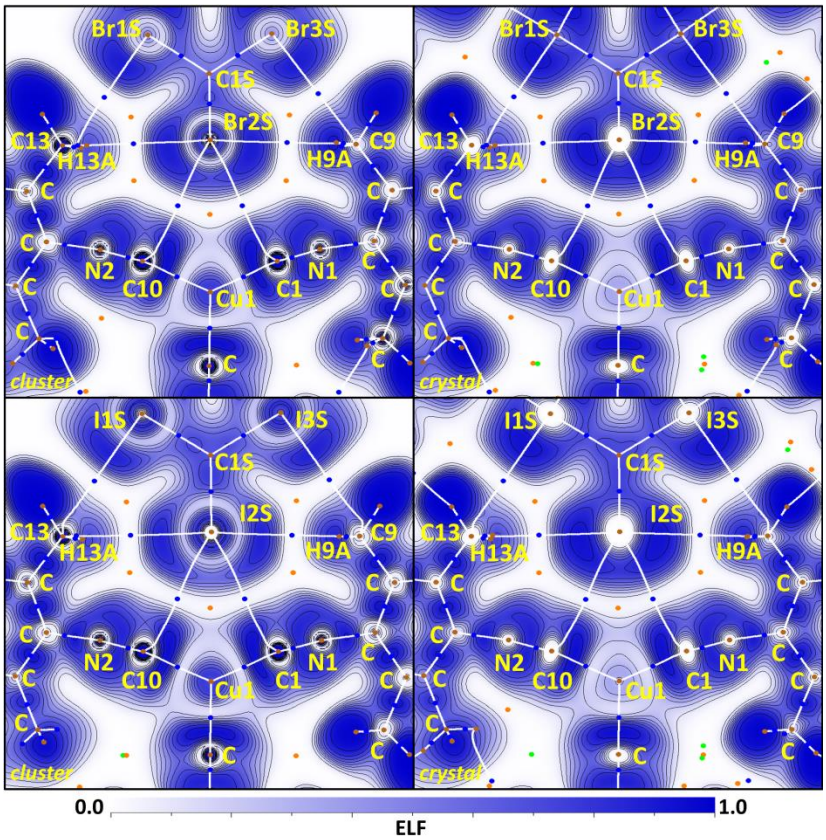

Figure S19. ELF projections (contour lines with 0.1 step) and bond paths (white lines), bond CPs (blue dots), nuclear CPs (brown dots), ring CPs (orange dots), and cell CPs (green dots), for the C1S−X2S···(C1,C10) BHaBs in the *cluster* (left) and *crystal* (right) models of $[CuI_3(CNXyl)_3]\cdot CHBr_3$ (upper) and $[CuI_3(CNXyl)_3]$ CHI_3 (lower).

The philicities of partners in other HaBs between haloforms and triiodide ligands can be also confirmed in the same way, as shown in **Figures S20–S21**.

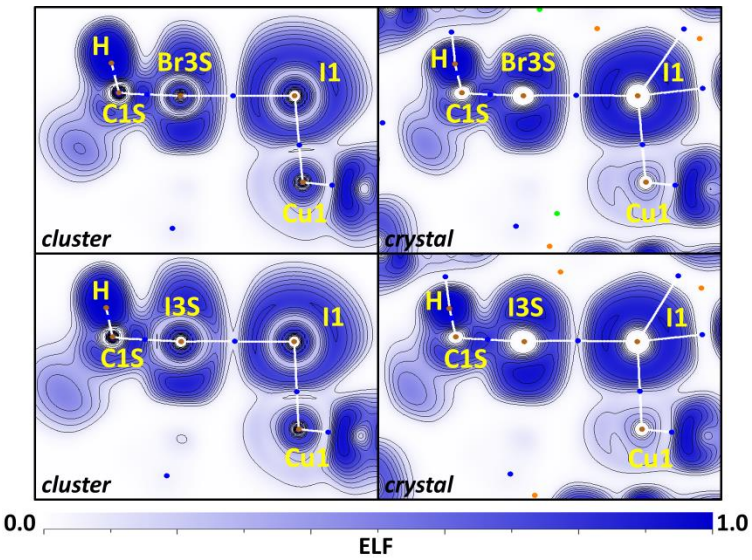

Figure S20. ELF projections (contour lines with 0.1 step) and bond paths (white lines), bond CPs (blue dots), nuclear CPs (brown dots), ring CPs (orange dots), and cell CPs (green dots), for the C1S−X3S···I1−Cu1 HaBs in the *cluster* (left) and *crystal* (right) models of $[CuI_3(CNXyl)_3]\cdot CHBr_3$ (upper) and $[CuI_3(CNXyl)_3]\cdot CHI_3$ (lower).

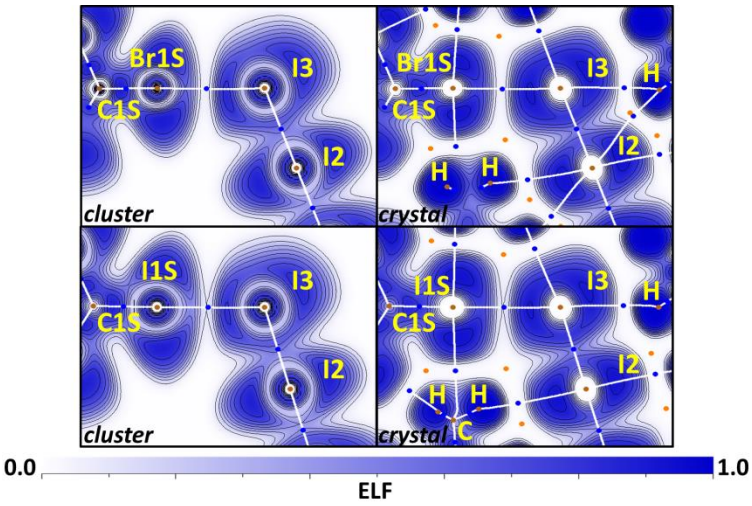

Figure S21. ELF projections (contour lines with 0.1 step) and bond paths (white lines), bond CPs (blue dots), nuclear CPs (brown dots), ring CPs (orange dots), and cell CPs (green dots), for the C1S−X1S···I3−I2 HaBs in the cocrystals.

Finally, overall electrophilicity of halomethane molecules toward complexes were confirmed by negative sums (−0.066 and −0.062 e for $CHBr_3$ and CHI_3, respectively) of halomethane RESP atomic charges in *crystal* models.

Calculations on models of [Na(Et$_2$O)][Co(CO)(CNAr)$_3$] and Na$_2$[Fe(CNAr)$_4$]

The XRD structures of the sodium salts [Na(Et$_2$O)][Co(CO)(CNAr)$_3$] (Ar = C$_6$H$_3$-2,6-(C$_6$H$_2$-2,4,6-Me$_3$)$_2$) and Na$_2$[Fe(CNAr)$_4$] (Ar = C$_6$H$_3$-2,6-(C$_6$H$_2$-2,4,6-Me$_3$)$_2$) are very crowded and therefore the ligands were simplified and the minimalistic isocyanobenzene was used instead, in order to be able to visualize the Na···(NC−M−CN) interaction in detail, which is the purpose of this study. Otherwise, a very complicated distribution of bond CPs and NCI/IRI/IGM plot isosurfaces appears that does not allow to envisage the noncovalent interactions.

In both models the QTAIM analysis shows a bond CP and bond path connecting the Na atom to the Co or Fe centers, thus disclosing the existence of Na···M (M = Co, Fe) interaction. The NCI (**Figure S22** a, c), IRI (main text, **Figure 6**) and IGM (**Figure S22** b, d) plots are quite similar, revealing a blue isosurface located between both metals and it originates from an attractive Na···M interaction. These analyses also indicate that the CN groups are mere spectators that are not involved in the Na···M interaction.

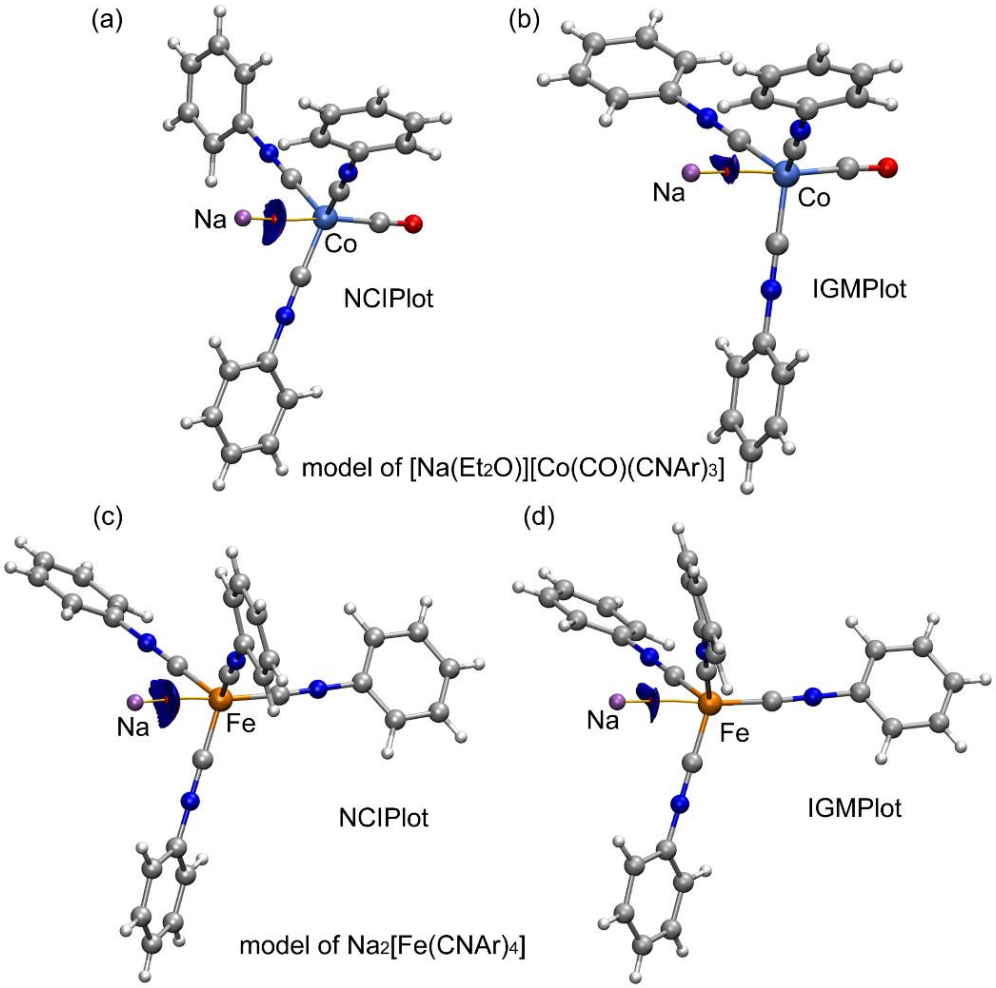

Figure S22. NCI (left) and IGM (right) plots of the reduced models of [Na(Et$_2$O)][Co(CO)(CNAr)$_3$] (top panel) Na$_2$[Fe(CNAr)$_4$] (bottom panel) at the PBE0-D3/def2-TZVP level of theory. Color scale used for the two plots –0.01 a.u. ≤ (signλ_2)ρ ≤ 0.01 a.u.

The results gathered in **Figures S16–S17** and **S22** clearly demonstrate that the physical nature of the (μ_2-X)···(NC−Cu−CN) interactions is totally different compared to that of the alkali metal cations, where the Na atom is connected to the Co/Fe metal center and the isosurface color is blue between the Na and the transition metal. It should be kept in mind that the main force in the alkali complexes is the electrostatic attraction between the cation and its anionic counterpart.

S6. References

1. G. M. Sheldrick, *Acta Crystallogr. Sect. A: Found. Crystallogr.*, 2008, **64**, 112-122.
2. O. V. Dolomanov, L. J. Bourhis, R. J. Gildea, J. A. K. Howard and H. Puschmann, *J. Appl. Crystallogr.*, 2008, **42**, 339-341.
3. C. Agilent, Agilent Technologies Ltd, Yarnton; Oxfordshire, 2014.
4. C. Adamo and V. Barone, *J. Chem. Phys.*, 1999, **110**, 6158–6170.
5. S. Grimme, J. Antony, S. Ehrlich and H. Krieg, *J. Chem. Phys.*, 2010, **132**, 154104.
6. F. Weigend, *Phys. Chem. Chem. Phys.*, 2006, **8**, 1057-1065.
7. M. J. Frisch, G. W. Trucks, H. B. Schlegel, G. E. Scuseria, M. A. Robb, J. R. Cheeseman, G. Scalmani, V. Barone, G. A. Petersson, H. Nakatsuji, X. Li, M. Caricato, A. V. Marenich, J. Bloino, B. G. Janesko, R. Gomperts, B. Mennucci, H. P. Hratchian, J. V. Ortiz, A. F. Izmaylov, J. L. Sonnenberg, Williams, F. Ding, F. Lipparini, F. Egidi, J. Goings, B. Peng, A. Petrone, T. Henderson, D. Ranasinghe, V. G. Zakrzewski, J. Gao, N. Rega, G. Zheng, W. Liang, M. Hada, M. Ehara, K. Toyota, R. Fukuda, J. Hasegawa, M. Ishida, T. Nakajima, Y. Honda, O. Kitao, H. Nakai, T. Vreven, K. Throssell, J. A. Montgomery Jr., J. E. Peralta, F. Ogliaro, M. J. Bearpark, J. J. Heyd, E. N. Brothers, K. N. Kudin, V. N. Staroverov, T. A. Keith, R. Kobayashi, J. Normand, K. Raghavachari, A. P. Rendell, J. C. Burant, S. S. Iyengar, J. Tomasi, M. Cossi, J. M. Millam, M. Klene, C. Adamo, R. Cammi, J. W. Ochterski, R. L. Martin, K. Morokuma, O. Farkas, J. B. Foresman and D. J. Fox, Wallingford, CT, 2016.
8. R. F. W. Bader, *Chem. Rev.* , 1991, **91**, 893-928.
9. E. R. Johnson, S. Keinan, P. Mori-Sánchez, J. Contreras-García, A. J. Cohen and W. Yang, *J. Am. Chem. Soc.*, 2010, **132**, 6498-6506.
10. J. Contreras-García, E. R. Johnson, S. Keinan, R. Chaudret, J.-P. Piquemal, D. N. Beratan and W. Yang, *J. Chem. Theory Comput.*, 2011, **7**, 625-632.
11. T. A. Keith, TK Gristmill Software, Overland Park KS, USA, 2019.
12. L. E. Zelenkov, D. M. Ivanov, E. K. Sadykov, N. A. Bokach, B. Galmés, A. Frontera and V. Y. Kukushkin, *Cryst. Growth Des.*, 2020, **20**, 6956-6965.
13. E. A. Katlenok, M. Haukka, O. V. Levin, A. Frontera and V. Y. Kukushkin, *Chem. Eur. J.*, 2020, **26**, 7692-7701.
14. S. V. Baykov, K. K. Geyl, D. M. Ivanov, R. M. Gomila, A. Frontera and V. Y. Kukushkin, *Chem. Asian J.*, 2021, **16**, 1445-1455.
15. Z. M. Efimenko, A. A. Eliseeva, D. M. Ivanov, B. Galmes, A. Frontera, N. A. Bokach and V. Y. Kukushkin, *Cryst. Growth Des.*, 2021, **21**, 588-596.
16. A. V. Rozhkov, I. V. Ananyev, A. A. Petrov, B. Galmes, A. Frontera, N. A. Bokach and V. Y. Kukushkin, *Cryst. Growth Des.*, 2021, **21**, 4073-4082.
17. V. V. Suslonov, N. S. Soldatova, D. M. Ivanov, B. Galmes, A. Frontera, G. Resnati, P. S. Postnikov, V. Y. Kukushkin and N. A. Bokach, *Cryst. Growth Des.*, 2021, **21**, 5360-5372.

18. Y. V. Torubaev, I. V. Skabitsky, A. V. Rozhkov, B. Galmes, A. Frontera and V. Y. Kukushkin, *Inorg. Chem. Front.*, 2021, **8**, 4965-4975.

19. L. E. Zelenkov, A. A. Eliseeva, S. V. Baykov, V. V. Suslonov, B. Galmes, A. Frontera, V. Y. Kukushkin, D. M. Ivanov and N. A. Bokach, *Inorg. Chem. Front.*, 2021, **8**, 2505-2517.

20. F. Weigend and M. Häser, *Theor. Chem. Acta*, 1997, **97**, 331-340.

21. A. Bauzá, I. Alkorta, A. Frontera and J. Elguero, *J. Chem. Theory Comput.*, 2013, **9**, 5201-5210.

22. F. Neese, *WIREs Comput. Mol. Sci.* , 2018, **8**, e1327.

23. T. Lu and Q. Chen, *Chem. Methods*, 2021, **1**, 231-239.

24. C. Lefebvre, H. Khartabil, J.-C. Boisson, J. Contreras-García, J.-P. Piquemal and E. Hénon, *ChemPhysChem*, 2018, **19**, 724-735.

25. C. Lefebvre, G. Rubez, H. Khartabil, J.-C. Boisson, J. Contreras-García and E. Hénon, *Phys. Chem. Chem. Phys.*, 2017, **19**, 17928-17936.

26. M. Ponce-Vargas, C. Lefebvre, J.-C. Boisson and E. Hénon, *J. Chem. Inf. Model.*, 2020, **60**, 268-278.

27. J. Klein, H. Khartabil, J.-C. Boisson, J. Contreras-García, J.-P. Piquemal and E. Hénon, *J. Phys. Chem. A*, 2020, **124**, 1850-1860.

28. T. Lu and F. W. Chen, *J. Comput. Chem.*, 2012, **33**, 580–592.

29. W. Humphrey, A. Dalke and K. Schulten, *J. Mol. Graph.*, 1996, **14**, 33-38.

30. R. Ahlrichs, M. Bär, M. Häser, H. Horn and C. Kölmel, *Chem. Phys. Lett.*, 1989, **162**, 165-169.

31. B. G. Lippert, J. H. Parrinello and Michele, *Molecular Physics*, 1997, **92**, 477-488.

32. J. P. Perdew, K. Burke and M. Ernzerhof, *Phys. Rev. Lett.*, 1996, **77**, 3865-3868.

33. S. Grimme, S. Ehrlich and L. Goerigk, *J. Comp. Chem.*, 2011, **32**, 1456–1465.

34. M. Frigo and S. G. Johnson, *Proc. IEEE*, 2005, **93**, 216-231.

35. J. VandeVondele, M. Krack, F. Mohamed, M. Parrinello, T. Chassaing and J. Hutter, *Comput. Phys. Commun.*, 2005, **167**, 103-128.

36. J. Hutter, M. Iannuzzi, F. Schiffmann and J. VandeVondele, *WIREs Comput. Mol. Sci.*, 2014, **4**, 15-25.

37. U. Borštnik, J. VandeVondele, V. Weber and J. Hutter, *Parallel Comput.*, 2014, **40**, 47-58.

38. O. Schütt, P. Messmer, J. Hutter and J. VandeVondele, in *Electronic Structure Calculations on Graphics Processing Units*, 2016, pp. 173-190.

39. L. Goerigk, A. Hansen, C. Bauer, S. Ehrlich, A. Najibi and S. Grimme, *Phys. Chem. Chem. Phys.*, 2017, **19**, 32184-32215.

40. T. D. Kühne, M. Iannuzzi, M. D. Ben, V. V. Rybkin, P. Seewald, F. Stein, T. Laino, R. Z. Khaliullin, O. Schütt, F. Schiffmann, D. Golze, J. Wilhelm, S. Chulkov, M. H. Bani-Hashemian, V. Weber, U. Borštnik, M. Taillefumier, A. S. Jakobovits, A. Lazzaro, H. Pabst, T. Müller, R. Schade, M. Guidon, S. Andermatt, N. Holmberg, G. K. Schenter, A. Hehn, A. Bussy, F. Belleflamme, G. Tabacchi, A. Glöß, M. Lass, I. Bethune, C. J. Mundy,

C. Plessl, M. Watkins, J. VandeVondele, M. Krack and J. Hutter, *J. Chem. Phys.*, 2020, **152**, 194103.

41. B. Silvi and A. Savin, *Nature*, 1994, **371**, 683-686.
42. A. Savin, R. Nesper, S. Wengert and T. F. Fässler, *Angew. Chem. Int. Ed.*, 1997, **36**, 1808-1832.
43. J. VandeVondele and J. Hutter, *J. Chem. Phys.*, 2007, **127**, 114105.
44. S. Goedecker, M. Teter and J. Hutter, *Phys. Rev. B* 1996, **54**, 1703-1710.
45. M. Krack, *Theor. Chem. Acc.*, 2005, **114**, 145-152.
46. C. Hartwigsen, S. Goedecker and J. Hutter, *Phys. Rev. B* 1998, **58**, 3641-3662.
47. C. Campañá, B. Mussard and T. K. Woo, *J. Chem. Theory Comput.*, 2009, **5**, 2866-2878.
48. D. Golze, J. Hutter and M. Iannuzzi, *Phys. Chem. Chem. Phys.*, 2015, **17**, 14307-14316.
49. D. Golze, M. Iannuzzi and J. Hutter, *J. Chem. Theory Comput.*, 2017, **13**, 2202-2214.
50. F. E. Oropeza, M. Barawi, E. Alfonso-González, V. A. de la Peña O'Shea, J. F. Trigo, C. Guillén, F. Saiz and I. J. Villar-Garcia, *J. Mater. Chem. C*, 2021, **9**, 11859-11872.
51. S. Wang, J. S. Lee, M. Wahiduzzaman, J. Park, M. Muschi, C. Martineau-Corcos, A. Tissot, K. H. Cho, J. Marrot, W. Shepard, G. Maurin, J.-S. Chang and C. Serre, *Nature Energy*, 2018, **3**, 985-993.
52. X.-D. Wang, Y.-H. Huang, J.-F. Liao, Y. Jiang, L. Zhou, X.-Y. Zhang, H.-Y. Chen and D.-B. Kuang, *J. Am. Chem. Soc.*, 2019, **141**, 13434-13441.
53. Y. G. Chung, E. Haldoupis, B. J. Bucior, M. Haranczyk, S. Lee, H. Zhang, K. D. Vogiatzis, M. Milisavljevic, S. Ling, J. S. Camp, B. Slater, J. I. Siepmann, D. S. Sholl and R. Q. Snurr, *J. Chem. Eng. Data*, 2019, **64**, 5985-5998.
54. Q. Bao, W. Zhang and D. Mei, *Phys. Chem. Chem. Phys.*, 2021, **23**, 23360-23371.
55. F. I. Pambudi and N. Prasetyo, *Mater. Today Commun.*, 2021, **26**, 102028.
56. A. Hazra, S. Bonakala, S. A. Adalikwu, S. Balasubramanian and T. K. Maji, *Inorg. Chem.*, 2021, **60**, 3823-3833.
57. K. Laasonen, E. Panizon, D. Bochicchio and R. Ferrando, *J. Phys. Chem. C*, 2013, **117**, 26405-26413.
58. S. P. Thomas, M. S. Pavan and T. N. Guru Row, *Chem. Commun.*, 2014, **50**, 49-51.
59. Y. V. Nelyubina, A. A. Korlyukov and K. A. Lyssenko, *ChemPhysChem*, 2015, **16**, 676-681.
60. S. Sarkar, M. S. Pavan and T. N. Guru Row, *Phys. Chem. Chem. Phys.*, 2015, **17**, 2330-2334.
61. M. S. Pavan, K. Durga Prasad and T. N. Guru Row, *Chem. Commun.*, 2013, **49**, 7558-7560.
62. Z. Chua, B. Zarychta, C. G. Gianopoulos, V. V. Zhurov and A. A. Pinkerton, *Acta Crystallogr., Sect. B*, 2017, **73**, 654-659.
63. I. Sovago, M. J. Gutmann, J. G. Hill, H. M. Senn, L. H. Thomas, C. C. Wilson and L. J. Farrugia, *Cryst. Growth Des.*, 2014, **14**, 1227-1239.

64. M. E. Brezgunova, E. Aubert, S. Dahaoui, P. Fertey, S. Lebègue, C. Jelsch, J. G. Ángyán and E. Espinosa, *Cryst. Growth Des.*, 2012, **12**, 5373-5386.

65. E. Aubert, S. Lebègue, M. Marsman, T. T. T. Bui, C. Jelsch, S. Dahaoui, E. Espinosa and J. G. Ángyán, *J. Phys. Chem. A*, 2011, **115**, 14484-14494.

66. A. Bondi, *J. Phys. Chem.*, 1964, **68**, 441–451.

67. S. Alvarez, *Dalton Trans.*, 2013, **42**, 8617-8636.

68. G. R. Desiraju, P. S. Ho, L. Kloo, A. C. Legon, R. Marquardt, P. Metrangolo, P. Politzer, G. Resnati and K. Rissanen, *Pure Appl. Chem.*, 2013, **85**, 1711-1713.

69. H. G. Loehr, A. Engel, H. P. Josel, F. Voegtle, W. Schuh and H. Puff, *J. Org. Chem.*, 1984, **49**, 1621-1627.

70. W.-W. du Mont, V. Stenzel, J. Jeske, P. G. Jones, A. Sebald, S. Pohl, W. Saak and M. Baetcher, *Inorg. Chem.* , 1994, **33**, 1502-1505.

71. H. Bock and S. Holl, *Z. Naturforsch. B*, 2001, **56**, 152-163.

72. B. Watson, O. Grounds, W. Borley and S. V. Rosokha, *Phys. Chem. Chem. Phys.*, 2018, **20**, 21999-22007.

73. S. V. Rosokha, I. S. Neretin, T. Y. Rosokha, J. Hecht and J. K. Kochi, *Heteroat. Chem.*, 2006, **17**, 449-459.

74. S. V. Rosokha and M. K. Vinakos, *Cryst. Growth Des.*, 2012, **12**, 4149-4156.

75. S. V. Baykov, U. Dabranskaya, D. M. Ivanov, A. S. Novikov and V. P. Boyarskiy, *Cryst. Growth Des.*, 2018, **18**, 5973-5980.

76. D. M. Ivanov, A. S. Novikov, I. V. Ananyev, Y. V. Kirina and V. Y. Kukushkin, *Chem. Commun.*, 2016, **52**, 5565-5568.

77. M. Bulatova, D. M. Ivanov and M. Haukka, *Cryst. Growth Des.*, 2021, **21**, 974-987.

78. K. Morimoto and T. Inabe, *Mol. Cryst. Liq.*, 1996, **284**, 291-300.

79. H. Hartl and S. Steidl, *Acta Crystallogr., Sect. B*, 1980, **36**, 65-69.

80. L. R. Nassimbeni, M. L. Niven and A. P. Suckling, *Inorg. Chim. Acta*, 1989, **159**, 209-217.

81. T. Dahl and O. Hassel, *Acta Chem. Scand.*, 1971, **25**, 2168-&.

82. C. Weinberger, R. Hines, M. Zeller and S. V. Rosokha, *Chem. Commun.*, 2018, **54**, 8060-8063.

83. T. Bjorvatt and O. Hassel, *Acta Chem. Scand.*, 1962, **16**, 249-&.

84. T. Dahl and O. Hassel, *Acta Chem. Scand.*, 1970, **24**, 377-&.

85. F. Bertolotti and G. Gervasio, *J. Mol. Struct.*, 2013, **1036**, 305-310.

86. T. Bjorvatten and O. Hassel, *Acta Chem. Scand.*, 1961, **15**, 1429-&.

87. T. Bjorvatten, *Acta Chem. Scand.*, 1962, **16**, 749-754.

88. D. J. Wolstenholme, K. N. Robertson, E. M. Gonzalez and T. S. Cameron, *J. Phys. Chem. A*, 2006, **110**, 12636-12643.

89. Z. T. Lu, Z. D. Sun, Y. Chi, H. G. Xue and S. P. Guo, *Inorg. Chem.* , 2019, **58**, 4619-4625.

90. L. E. Zelenkov, A. A. Eliseeva, S. Baykov, V. V. Suslonov, B. Galmés, A. Frontera, V. Y. Kukushkin, D. M. Ivanov and N. A. Bokach, *Inorg. Chem. Front.*, 2021, **8**, 2505-2517.

91. K. F. Dziubek and A. Katrusiak, *J. Phys. Chem. B*, 2008, **112**, 12001-12009.

92. D. S. Yufit, R. Zubatyuk, O. V. Shishkin and J. A. K. Howard, *CrystEngComm*, 2012, **14**, 8222-8227.

93. F. Bertolotti, N. Curetti, P. Benna and G. Gervasio, *J. Mol. Struct.*, 2013, **1041**, 106-112.

94. J. P. Wojciechowski, A. D. Martin, M. Bhadbhade, J. E. A. Webb and P. Thordarson, *CrystEngComm*, 2016, **18**, 4513-4517.

95. D. S. Yufit, O. V. Shishkin, R. I. Zubatyuk and J. A. K. Howard, *Cryst. Growth Des.*, 2014, **14**, 4303-4309.

96. D. S. Yufit, O. V. Shishkin, R. I. Zubatyuk and J. A. K. Howard, *Z. Kristallogr. Cryst. Mater.*, 2014, **229**, 639-647.

97. R. Thaimattam, F. Xue, J. A. R. P. Sarma, T. C. W. Mak and G. R. Desiraju, *J. Am. Chem. Soc.*, 2001, **123**, 4432-4445.

98. T. Bjorvatten, *Acta Chem. Scand.*, 1963, **17**, 2292-&.

99. E. Espinosa, E. Molins and C. Lecomte, *Chem. Phys. Lett.*, 1998, **285**, 170-173.